Multiphoton-Excited Fluorescence of Silicon-Vacancy Color Centers in Diamond

J. M. Higbie,[1,*] J. D. Perreault,[1] V. M. Acosta,[2] C. Belthangady,[1] P. Lebel,[1,†] M. H. Kim,[1] K. Nguyen,[1] V. Demas,[1] V. Bajaj,[1] and C. Santori[1]

[1]*Verily Life Sciences, South San Francisco, California 94080, USA*
[2]*University of New Mexico, Albuquerque, New Mexico 87106, USA*

(Received 27 September 2016; revised manuscript received 1 March 2017; published 15 May 2017)

Silicon-vacancy color centers in nanodiamonds are promising as fluorescent labels for biological applications, with a narrow, nonbleaching emission line at 738 nm. Two-photon excitation of this fluorescence offers the possibility of low-background detection at significant tissue depth with high three-dimensional spatial resolution. We measure the two-photon fluorescence cross section of a negatively charged silicon vacancy (Si-V^-) in ion-implanted bulk diamond to be $0.74(19) \times 10^{-50}$ cm^4 s/photon at an excitation wavelength of 1040 nm. Compared to the diamond nitrogen-vacancy center, the expected detection threshold of a two-photon excited Si-V center is more than an order of magnitude lower, largely due to its much narrower linewidth. We also present measurements of two- and three-photon excitation spectra, finding an increase in the two-photon cross section with decreasing wavelength, and we discuss the physical interpretation of the spectra in the context of existing models of the Si-V energy-level structure.

DOI: 10.1103/PhysRevApplied.7.054010

I. INTRODUCTION

Color centers in diamond have been the focus of intense interest in recent years. The nitrogen-vacancy (N-V) color center in diamond has driven much of this interest, thanks to numerous promising applications, including nanoscale magnetometry [1–5], NMR spectroscopy [6,7], quantum information [8–13], and fluorescent biolabeling [14,15]. More recently, the silicon-vacancy (Si-V) color center in diamond, which has been known for over two decades [16–18], has generated increasing excitement [19–23] because of properties that are, in some respects, even more favorable than those of the nitrogen-vacancy defect, such as a narrow zero-phonon line (ZPL) [16] and weak phonon sidebands at room temperature [24]. This concentrated emission in a narrow ZPL allows detection of silicon-vacancy-containing diamonds at higher signal-to-noise ratios, and it raises the possibility that silicon-vacancy-doped nanodiamonds bound to specific biomolecular targets could be detectable in the presence of a high autofluorescence background, e.g., in deep and/or highly scattering biological tissue.

Specifically targeted nanoparticle probes that can be detected through millimeters of intervening tissue promise to be an enabling technology for minimally invasive *in vivo* molecular imaging, with potential applications in biomarker discovery, studies of immune-cell trafficking and circulating tumor cells, elucidation of molecular pathways in preclinical models, drug development, and, ultimately in clinical diagnosis. Toward these ends, various combinations of nanoparticle type and detection modality have been investigated, including superparamagnetic nanoparticles detected via magnetic resonance imaging [25], fluorescence imaging of dyes [26], quantum dots [27,28], and nanodiamonds [29,30], and surface-enhanced Raman particles [31,32].

Two-photon excited fluorescence imaging is particularly appealing for deep-tissue imaging because of its high spatial resolution, natural longitudinal sectioning, and low background, and because the longer excitation wavelengths typically used allow enhanced penetration and lower phototoxicity in tissue [33]. These advantages have led to significant application of two-photon imaging in neuroscience [34], and they will likely be important in other areas involving high-spatial-resolution imaging through scattering tissue. While two-photon labels such as organic dyes and fluorescent proteins achieve very high brightness [35,36], Si-V centers are likely to offer distinct advantages thanks to their narrow emission bandwidth and lack of bleaching. A further unique feature of the silicon-vacancy color center is the circumstance that the excitation can be within the second near-IR transmission window of tissue (around 1040 nm) and the emission (around 738 nm) within the first transmission window (see, e.g., Ref. [37]). Song *et al.* [38] have previously observed a quadratic dependence of 830-nm-excited silicon vacancies coupled to the plasmon resonances of gold nanoellipsoids, attributable to two-photon excitation. A quantitative measure of the strength of two-photon-excited fluorescence, however, has not previously been obtained for the Si-V defect. Here, we present the first report of the two-photon fluorescence cross section of the negatively charged silicon vacancy (Si-V^-) color

*jhigbie@google.com
†Present address: Berkeley Lights, Emeryville, CA 94608, USA.

center in diamond. Based on the results, we evaluate the prospects of Si-V nanodiamond as a contrast agent for biological labeling applications, particularly for *in vivo* and deep-tissue imaging, where strong background fluorescence and low photon collection efficiency must be overcome.

II. BACKGROUND

The structure of the Si-V^- color center has been elucidated in recent years in a number of works [18–20,22,39]. The color center consists of a single silicon atom located midway between two adjacent vacant carbon lattice sites (vacancies), as shown in Fig. 1; this configuration possesses trigonal D_{3D} symmetry. A level diagram tentatively suggested by Rogers *et al.* [19] is given in Fig. 1, showing ground and excited states relevant to this work. Excitation of the defect from the ^2E_g ground state to the ^2E_u excited state can be achieved either directly or indirectly via higher-lying levels such as the $^2A_{1g}$ state, combined with subsequent (presumed nonradiative) relaxation. The defect then returns to the ground state by emission of a 1.68-eV (738-nm) photon. An unusually large portion of the emitted radiation is in the narrow zero-phonon line, improving the signal-to-noise ratio with which the color center can be detected.

The two-photon fluorescence cross section σ_{2p} for a single point-fluorophore is defined by the relation

$$\langle \Gamma \rangle = \sigma_{2p} \langle I^2 \rangle, \tag{1}$$

where Γ is the fluorescence photon-emission rate, I is the excitation intensity at the fluorophore (conventionally measured in units of photon number per area per length of time), and angle brackets indicate time averaging over an interval significantly greater than the excited-state decay time. In practice, one measures not the total emission

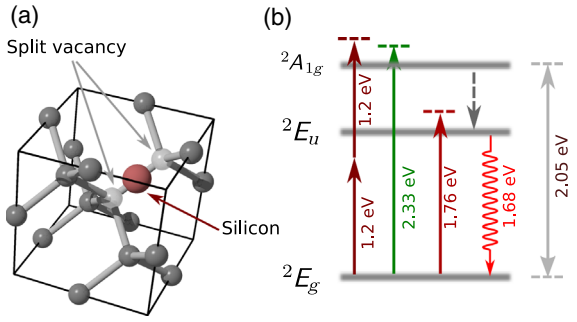

FIG. 1. (a) Diamond unit cell containing a silicon-vacancy lattice defect, consisting of a silicon nucleus midway between two vacant nearest-neighbor lattice sites. (b) The simplified level diagram of the negatively charged silicon-vacancy color center in diamond, showing states and optical transitions relevant to this work, with excitation via two-photon absorption at 1040 nm (1.19 eV) or one-photon absorption at either 705 nm (1.76 eV) or 532 nm (2.33 eV).

rate, but the quantity $\Gamma_{det} \equiv \eta_{det} \langle \Gamma \rangle$, where the detection efficiency η_{det} includes the fraction of light collected by the microscope objective and the transmission of all optical components in the detection path.

Because a pulsed laser must typically be used to obtain appreciable two-photon-excited fluorescence, we must further relate the mean-square intensity appearing in Eq. (1) to the more readily measurable mean intensity. Specifically, we consider excitation via a periodic pulse train with a temporal profile that is well approximated by a sum of Gaussian-envelope pulses,

$$I_0(t) = I_{peak} \sum_{n=-\infty}^{\infty} \exp[-(t - nT_{rep})^2/\tau^2], \tag{2}$$

where I_0 is the intensity at the laser focus, I_{peak} is the temporal-peak intensity, T_{rep} is the repetition period, and τ defines the pulse width. The time average of the intensity and the square intensity over a time span that is long compared to the repetition period, neglecting the overlap of distinct pulses, are readily calculated by integration and obey the relation

$$\langle I_0^2 \rangle = \langle I_0 \rangle^2 \frac{T_{rep}}{\tau\sqrt{2\pi}}. \tag{3}$$

Moreover, the intensity I_0 at the laser focus is related to the total laser power by

$$P = \int dxdy I(x,y) \equiv I_0 A_{ex}. \tag{4}$$

Here, A_{ex} is the area defined by the excitation point-spread function $F_{ex}(x,y)$, i.e.,

$$A_{ex} \equiv \int dxdy F_{ex}(x,y), \tag{5}$$

with the unit-maximum point-spread function $F_{ex}(x,y)$ defined, in turn, by the relation $I(x,y) = I_0 F_{ex}(x,y)$.

Thus, for such a pulse train, the average detection rate of photons emitted by a single color center at the focus of the laser beam is given by

$$\Gamma_{det,2p} = \eta_{det} \sigma_{2p} \langle I_0^2 \rangle \tag{6}$$

$$= \eta_{det} \sigma_{2p} \langle I_0 \rangle^2 \frac{T_{rep}}{\tau\sqrt{2\pi}}, \tag{7}$$

where the time-averaged intensity at the focus is given in terms of the time-averaged excitation power $\langle P \rangle$ by $\langle I_0 \rangle = \langle P \rangle / A_{ex}$. For an isolated color center, then, the two-photon cross section is related to measurable quantities by the equation

$$\Gamma_{\mathrm{det},2p} = \eta_{\mathrm{det}}\sigma_{2p}\left(\frac{\langle P\rangle}{A_{\mathrm{ex}}}\right)^2 \frac{T_{\mathrm{rep}}}{\tau\sqrt{2\pi}} S_P, \tag{8}$$

where S_P is an empirically determined saturation factor (described more fully below) accounting for any deviation of the intensity dependence from the strictly quadratic dependence of Eq. (1).

III. EXPERIMENTAL APPARATUS

The experimental apparatus (illustrated in Fig. 2) consists of a two-photon epifluorescence microscope to excite and detect silicon-vacancy color centers in a diamond sample. Excitation light is derived from a mode-locked 1040-nm ytterbium fiber laser (Menlo Orange) producing 144-fs (full width at $1/e$ of maximum) pulses at a repetition rate of 100 MHz, with an average power of around 300 mW. The excitation light is focused via a 40×, NA = 0.75 air-spaced objective into a diamond sample mounted on a three-axis closed-loop translation stage (Newport VP-25XL and XPS controller). Two-photon-excited fluorescence from the sample is collected and collimated by the objective, reflected from a dichroic beam splitter, filtered by long-pass and bandpass filters, and refocused onto a scientific CMOS (sCMOS) camera (Hamamatsu Orca Flash4.0) or, alternatively, free space coupled to a spectrograph (Princeton Instruments Acton SP2500) for a spectral analysis of the emitted light.

We employ samples consisting of bulk diamond implanted with silicon ions and annealed to produce silicon vacancies and minimize undesired defects. High-purity CVD-grown single-crystal diamond chips (< 5 ppb

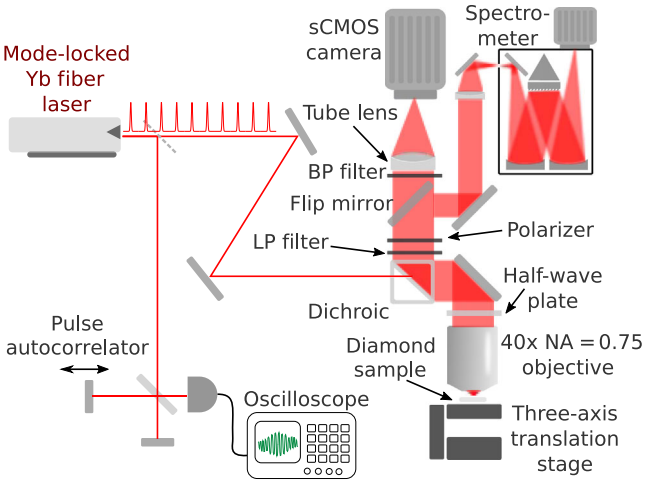

FIG. 2. Diagram of the two-photon epifluorescence apparatus showing the diamond sample illuminated by the pulsed two-photon excitation laser beam at 1040 nm or by one of two one-photon excitation laser beams, with detection by a sCMOS camera or an imaging spectrometer. An autocorrelator allows measurement of the two-photon laser-pulse width. BP and LP denote band-pass and long-pass filters respectively.

nitrogen, Element Six), are Si-ion implanted (Materials Diagnostics, Albany, New York), with the implantation energies chosen to achieve the desired depth profile, as calculated by the stopping range of ions in matter (SRIM) software [40]. The implantation surface is a (100) plane of the diamond crystal. Low-density samples for the observation of single color centers are fabricated at an implantation density of 5×10^9 ions/cm^2 and an ion energy of 3 MeV, while high-density samples for an improved signal-to-noise measurement ratio are fabricated at implantation densities from 10^{12} ions/cm^2 to 10^{15} ions/cm^2 with a selection of energies between 500 keV and 3 MeV designed to produce approximately uniform Si-V density over the first micrometer of subsurface crystal depth. After implantation, the samples are annealed in vacuum by ramping over 2 h to 400 °C and holding for 4 h, then ramping over 2 h to 800 °C and holding for 4 h, before ramping back to room temperature.

Isolated single–Si-V color centers are located in the low-density samples by raster scanning the sample in the plane transverse to the optical axis. A comparison between one-photon fluorescence microscopy of the Si-V centers with a large digital confocal pinhole and surface-reflection depth scans using the same 705-nm laser beam indicates that the color centers are within approximately 1 μm of the diamond surface, as expected from the simulations. A polarizer is placed in the imaging path following the dichroic mirror to allow analysis of the polarization direction of the emitted light, and a half-wave plate is mounted in a computer-controlled rotation stage immediately above the objective. As we observe no dependence of the emitted light intensity on the excitation polarization with the polarizer omitted, rotating the wave plate is considered equivalent to rotating the transmission axis of the polarizer, but with the advantage of holding the detected polarization axis constant throughout the downstream imaging system and spectrometer.

The power of the two-photon excitation beam is measured using a slide-format thermal power meter (Thorlabs S175C) placed in the position normally occupied by the sample. The excitation point-spread functions for the one- and two-photon beams are measured by scanning a single color center through the laser focus and recording a photoluminescence (PL) map, as shown in Fig. 3. Detection point-spread functions are determined by centering a color center on the laser focus and recording a long exposure (approximately 10 s) on the camera using a long-pass filter and a narrow bandpass filter to reject any residual excitation light reflected by the dichroic beam splitter.

The pulse width of the two-photon excitation laser is measured by means of a homebuilt autocorrelator consisting of a scanning Michelson interferometer with a (Ga,As)P photodiode at its output port. The (Ga,As)P band gap of 1.98 eV is larger than the single-photon energy at 1040 nm, and the photodiode output is proportional to the square of the incident power. The quantity of glass traversed by the

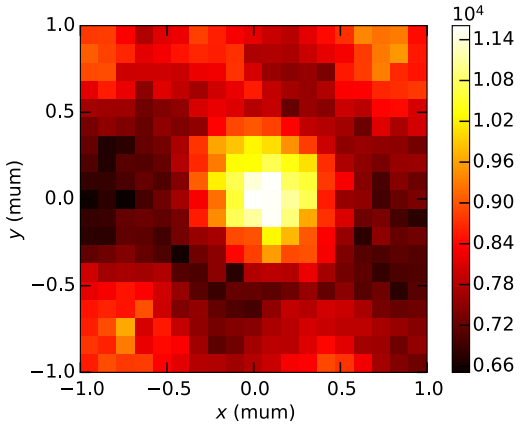

FIG. 3. Representative two-photon-excited photoluminescence image of a single silicon-vacancy defect obtained by scanning the sample through the 1040-nm pulsed excitation laser-beam focus and imaging the emitted fluorescence through a 13-nm-wide bandpass filter centered at 740 nm onto the sCMOS camera. Each pixel in the image represents the total counts collected by the camera within a digitally defined "pinhole" approximately 10 times larger than the imaging point-spread function.

laser beam before impinging on the sample is sufficiently small to lead us to expect negligible dispersion and pulse broadening at the sample; this expectation is confirmed by the experimental introduction of a glass component of comparable thickness prior to the autocorrelator, which is not found to produce detectable broadening of the pulse. The repetition rate is separately measured on an oscilloscope using the laser's synchronous radio-frequency output.

We further investigate the spectral dependence of the two-photon cross section using the signal output of a tunable optical parametric oscillator (Coherent Chameleon Compact OPO). The OPO signal wavelength is tuned under computer control over the range 1010–1550 nm, and fluorescence is detected at 738 nm. Making separate use of the remotely tunable titanium-sapphire pump laser allows us to extend the excitation range down to 920 nm, limited by our dichroic beam splitter. For these measurements, we employ an NA = 0.95, 100× objective corrected for use in the IR. The pulse width of the excitation laser beam is determined as a function of wavelength using the autocorrelator, substituting a silicon photodiode for the (Ga,As)P detector for wavelengths beyond 1300 nm. The excitation power is determined by measuring it in transmission using a large-area thermal power meter placed directly beneath the diamond sample and the underlying microscope slide. The analog output of the power meter is recorded via a data-acquisition system for each measurement, and a dark power-meter reading is also recorded at regular intervals during the measurement sequence by shuttering the excitation beam and waiting for the power-meter reading to stabilize. A half-wave plate in a computer-controlled rotator followed by a polarizing beam splitter allows us to vary the excitation power for each wavelength. To focus the imaging system, we introduce a weak laser beam at 736 nm into the excitation path via a pellicle beam splitter; the imaging system is periodically focused on the diamond surface by maximizing the peak intensity of the reflected 736-nm beam on the camera with the pulsed excitation light shuttered. At all other times, the 736-nm laser beam is itself shuttered. For our excitation-spectroscopy measurements, a 50:50 beam splitter is employed in place of the flipper mirror, allowing a simultaneous measurement of the emission spectrum and the two-dimensional excitation-beam profile.

IV. RESULTS

We determine the silicon-vacancy two-photon cross section σ_{2p} via Eq. (8), with all terms apart from σ_{2p} determined from experimentally measured quantities. In order to obtain reliable statistics on single-color-center emitters, we perform automated coarse, large-area scans of the transverse (x-y) position. Candidate Si-V centers are identified by means of the narrow ZPL at approximately 738 nm (with a median width of 5.6 nm FWHM for our samples), as shown in Fig. 4. When the spectral power in a window surrounding the ZPL exceeds the background in this window by an empirically determined threshold of 10%, the position of the candidate color center in the focus of the excitation beam is then optimized by sequential linear scans in the x, y, and z directions. When this optimization routine terminates successfully (i.e., with an above-threshold brightness and at a position not on the

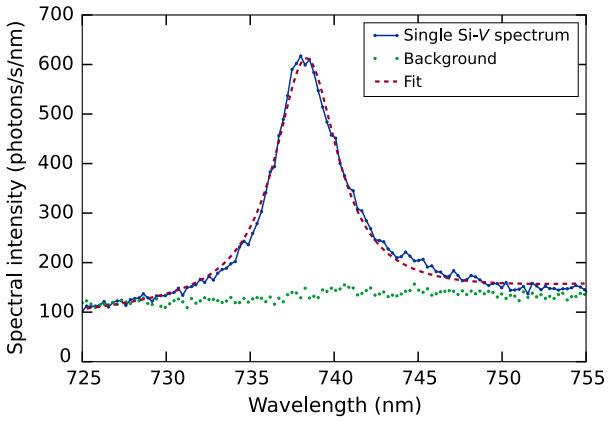

FIG. 4. Measured spectrum of a single two-photon-excited Si-V color center (the solid line and points). The color center is illuminated by 132 mW of laser power at 1040 nm, with a repetition rate of 100 MHz and a pulse duration $2\tau = 144$ fs (full width at $1/e$ of maximum). The spectrometer acquisition time is 30 s. A spectrum at a location 2 μm distant (the dotted line), not containing any color center, is shown below to indicate the spectral background. The red dashed curve is a fit to a Lorentzian with a second-order-polynomial background. The measured width of the Si-V ZPL is 4.6 nm.

boundary of the linear scans), the polarization contrast of the emitted light is then measured by recording spectra as a function of the wave-plate angle. Polarization curves for 162 distinct color centers are extracted from the raw spectrometer data by fitting each Si-V ZPL spectrum to a Lorentzian with a first-order polynomial background to obtain the area under the ZPL spectrum. Representative polarization curves are shown in Fig. 5. Individual Si-V centers may be aligned along any of four allowed axes (the unoriented body diagonals of the cubic diamond unit cell); the projection of the Si-V axis on the plane transverse to the imaging axis can, therefore, be aligned along two orthogonal directions which, for our sample, are parallel to the edges of the rectangular diamond chip and to the principal axes of the detection polarizer. Consequently, we expect individual Si-V centers to fall into two classes, with orthogonal emitted polarizations. Indeed, we observe that approximately half of the Si-V centers identified in a large scan have a maximum detection rate when the slow axis of the half-wave plate is set to an angle close to 0°, and approximately half have a maximum at an angle around 45°, corresponding to emission polarizations at angles of 0° and 90°, respectively. The polarization dependence and the spectral width are consistent with those reported for the Si-V defect in other studies [19,41–43].

The total ZPL photon count rate for each Si-V center is then taken to be the peak-to-peak amplitude of a cosine-squared fit to the polarization curve. This count rate displays a somewhat wide distribution, as shown in Fig. 6. We confirm via Monte Carlo simulations that a distribution of approximately this width is expected due to

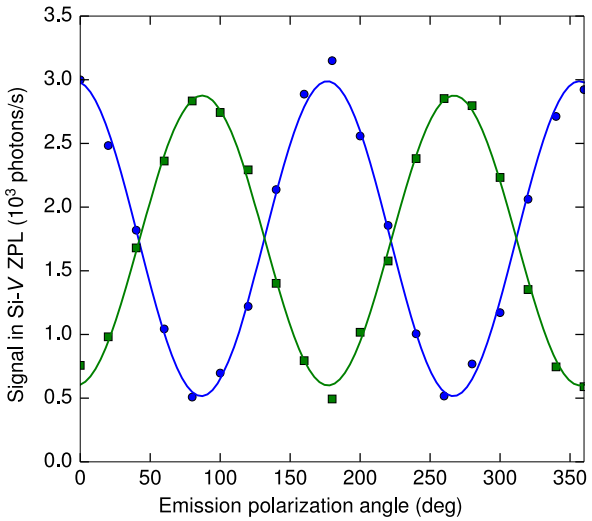

FIG. 5. Polarization dependence of emitted Si-V two-photon-excited fluorescence. The data (solid squares and circles) are obtained from two representative color centers, inferred to be oriented along crystal axes with orthogonal projections on the image plane. The solid lines are sinusoidal fits to the respective data. The measured count rate is the area under the ZPL curve, in units of photons per second incident on the spectrometer camera.

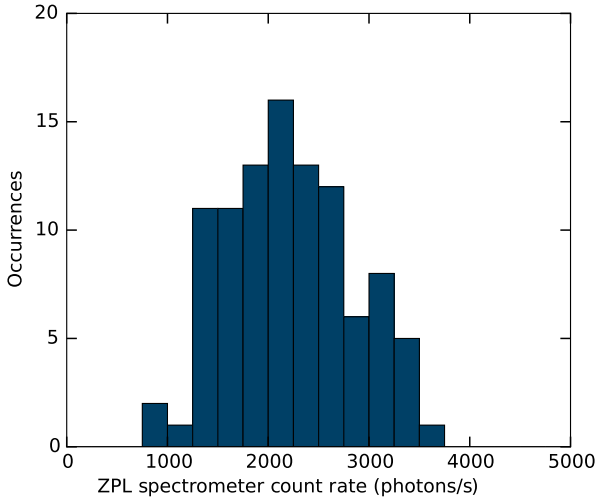

FIG. 6. Brightness distribution of individual Si-V color centers obtained from sinusoidally fitting polarization-dependent spectrometer ZPL count rates. We reject from this distribution defects with nearly twice the median brightness or with much lower polarization contrast, presumed to correspond to double Si-V centers with parallel or orthogonal projected orientations, respectively.

fluctuations in the number of color centers contributing to the signal. Indeed, while the number of color centers contributing to a single measurement is close to 1, the polarization curves in some cases receive non-negligible contributions from nearby color centers. Color centers with parallel dipole-emission axes tend to enhance the amplitude of the polarization curve, while those with orthogonal dipole-emission axes tend to reduce the contrast. The extreme cases of two color centers very close together with parallel or perpendicular emission axes can be excluded by rejecting candidate color centers whose polarization curves have exceptionally low contrast or exceptionally large amplitudes (specifically, amplitudes close to twice the typical single-Si-V amplitude). After excluding color centers with low contrast (40 of the 162 candidate centers) or anomalously high amplitudes (20 of the candidate centers), the median peak-to-peak amplitude is taken as the value of the ZPL detection count rate. The uncertainty in this value is dominated by the uncertainty of the spectrometer intensity calibration, so that, in practice, excluding these centers has a negligible effect on our result.

The saturation factor S_P is determined by varying the excitation power incident on a single Si-V color center centered on the laser focus in three dimensions and recording the detected ZPL fluorescence. Results of one such measurement are shown in Fig. 7. These data are empirically well fit by the functional form

$$\Gamma(P) \propto S_P P^2 = \frac{P^2}{1 + (P/P_{\mathrm{sat}})^2}, \tag{9}$$

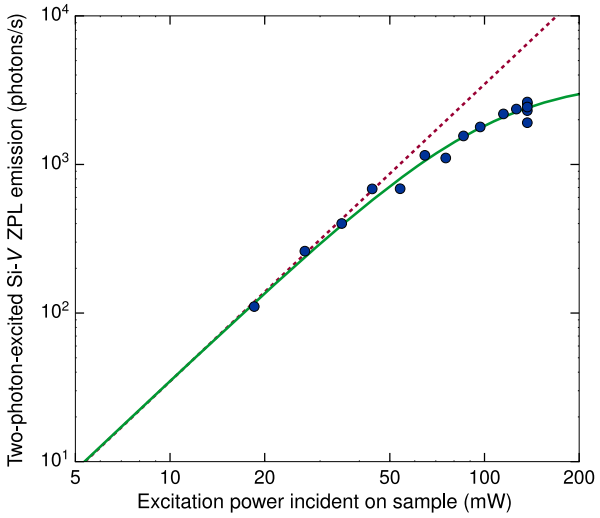

FIG. 7. Power dependence of the observed two-photon-excited ZPL fluorescence signal from a single isolated silicon vacancy. The solid circles are the measured data. The dashed line is a fit to pure quadratic dependence, while the solid line is the result of a curve fit including saturation.

where Γ is the detection rate at power P and P_{sat} is a time-averaged saturation power. For the measured beam shape, the fitted saturation power corresponds to a saturation intensity of 8.3×10^9 mW/cm^2, with a saturation count rate of 3.8×10^3 photons/s incident on the spectrometer camera. We point out that this count rate is limited in our system by the fact that a silicon vacancy can emit photons only every laser repetition period of approximately 10 ns, rather than every excited-state lifetime of approximately 1 ns. Taking this difference into account, our saturation count rate is comparable to the one-photon Si-V saturation rate of 56×10^3 counts/s measured by Rogers *et al.* [44] for an air-spaced objective. From analysis of our saturation measurements, we determine the saturation factor at the power used for the cross-section measurements to be $S_P = 0.36$. For a diamond sample containing many Si-V centers per excitation volume, the saturation behavior given by Eq. (9) is modified because color centers in the center of the beam experience a higher laser intensity and, therefore, saturate before those on the periphery. Assuming a Gaussian laser intensity profile, the expected saturation behavior for a dense sample can be calculated analytically by averaging Γ over spatial locations, the result being

$$\Gamma(P) \propto P_{\mathrm{sat}}^2 \log\left(1 + P^2/P_{\mathrm{sat}}^2\right). \tag{10}$$

The saturation behavior for a dense sample is also measured and fit using Eq. (10), and a consistent saturation intensity is obtained. Non-negligible saturation of the two-photon-excited fluorescence also changes the spatial profile of the PL map obtained by scanning the sample in the x-y plane. At low intensity, the PL map is expected to have a width approximately $\sqrt{2}$ smaller than the actual excitation intensity distribution, assuming a near-Gaussian beam profile, as a result of the quadratic dependence of scattering on intensity. For finite intensity, however, this factor is reduced; at the saturation factor $S_P = 0.36$ noted above, the width of the PL map is found numerically to be a factor of approximately 1.29 smaller than the actual beam width, but it is still reasonably well approximated by a Gaussian profile. Analysis of the transverse point-spread function (PSF) including this saturation behavior indicated a transverse excitation-beam width approximately 20% larger than the diffraction-limited value.

Calibration of the detection efficiency of our imaging system is performed using light from a diode laser at 736 nm, with which we measure the reflection or transmission coefficients of each element in the imaging beam path. Intensity calibration of the spectrometer camera at the operating temperature of −75 °C is performed using the light from the same laser beam with separately calibrated neutral-density filters, and it agrees with the manufacturer's value to within approximately 12%. The collection efficiency of the objective (including Fresnel reflection from the diamond-air interface) is calculated using its numerical aperture and the known refractive index of diamond (see Appendix A).

Analysis of our measured data yields a value of $\sigma_{2p,1040\ \mathrm{nm}} = 0.74(19)$ GM for the two-photon fluorescence cross section of a single Si-V center at 1040 nm, where the Goeppert-Mayer (GM) is the unit of two-photon cross section, equal to 10^{-50} cm^4 s/photon. The contributions of the various sources of uncertainty to our cross-section measurement are tabulated in Table I. Where possible, the uncertainty of each quantity is estimated as the standard deviation of repeated measurements. The uncertainty in the intensity calibration of the spectrometer is limited by the uncertainty in the power of the calibrating laser beam, which in turn is estimated by comparing the

TABLE I. Principal contributors to the error budget for the absolute measurement of Si-V σ_{2p} with excitation at 1040 nm and detection on the ZPL at 738 nm. The reported error in each quantity is an estimated single standard deviation. The total uncertainty is the sum in quadrature of the partial uncertainties. Symbols are as defined in the text.

Measured quantity	Value	Partial uncertainty (10^{-2} GM)
η_{det}	$4.04(35) \times 10^{-3}$	6.4
$\Gamma_{\mathrm{det},2p}$	$2.15(26) \times 10^3$ s^{-1}	8.9
τ	72.0(3.5) fs	3.6
A_{ex}	$8.79(77) \times 10^{-13}$ m^2	12.9
$\langle P \rangle$	101.5(3.8) mW	5.5
S_P	0.355(20)	4.2
Total:		19.0

measurements of two power meters after correcting for their wavelength dependence. The largest contribution to the uncertainty of the measurement is from imperfect knowledge of the excitation laser-beam shape at the sample, whose measurement is, in turn, limited by residual drift between the objective and translation stage. This uncertainty is estimated from the distribution of beam radii across the ensemble of single color centers, extracted by scanning each color center through the laser focus and measuring the emitted fluorescence. Color centers whose photoluminescence profile is not well fit by a single peak are excluded in the determination of this area.

The results of our excitation-spectroscopy measurements on a high-density Si-V sample are shown in Fig. 8. For each wavelength, we determine the photon detection rate as well as the two-dimensional spatial profile of the sample fluorescence as functions of excitation power. The photon count rate is extracted from the calibrated spectrometer signal by fitting the ZPL signal to a Lorentzian with a first-degree-polynomial background. For wavelengths below 1300 nm, the power dependence of the photon count is fit with good agreement to a function of the form of Eq. (10) to account for a small degree of saturation at shorter wavelengths. For wavelengths above 1300 nm, this fit function no longer gives satisfactory agreement, and instead a cubic fit polynomial is required to obtain good agreement with the power dependence. We interpret this dependence as indicating that for wavelengths above approximately 1300 nm, three-photon absorption begins to make a contribution comparable to that of two-photon absorption. At no wavelength in the range employed do we observe significant linear dependence on excitation intensity. The square of the unit-maximum-normalized excitation-beam spatial profile F_{ex}^2 is determined directly from the background-subtracted camera image of the photoluminescence, allowing us to calculate the effective beam areas $A_2 \equiv \int F_{\mathrm{ex}}^2 dA$, $A_{\mathrm{ex}} \equiv \int F_{\mathrm{ex}} dA$, and $A_3 \equiv \int F_{\mathrm{ex}}^3 dA$. The effect of saturation on these effective beam areas is accounted for by fitting A_2, A_3, and A_{ex} as linear functions of the square of the excitation power; the saturation-independent area in each case is taken to be the zero-power intercept of this fit. From the quadratic and cubic terms in our power-dependence fit results, combined with the other excitation-wavelength-dependent factors (excitation power, effective beam areas, and pulse width), we extract the two-photon and three-photon cross sections shown in Fig. 8. The product of the two-dimensional Si-V density $n_{2\mathrm{D}}$ and the detection efficiency η_{det} at 738 nm, which is common to the expressions for the two- and three-photon spectra, is chosen to normalize the two-photon cross section to our absolute measurement on single Si-V centers at 1040 nm.

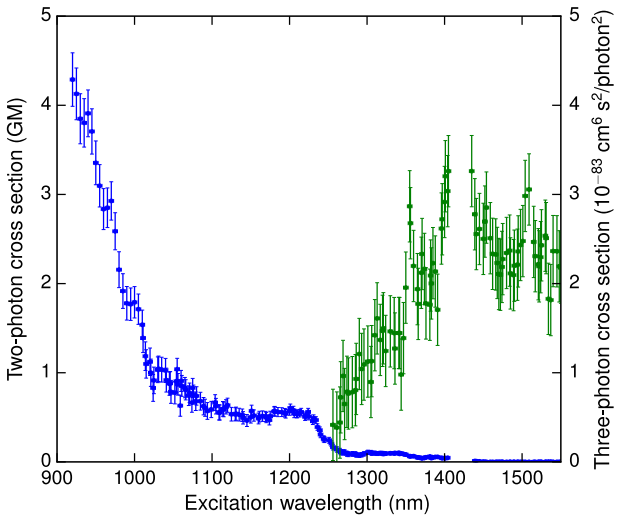

FIG. 8. Two- and three-photon-excited fluorescence spectra (left and right axes, respectively) of a diamond sample densely populated with Si-V color centers. Vertical error bars represent statistical uncertainties (standard deviations) of the corresponding two- and three-photon fluorescence cross sections. A gap between 1405 and 1435 nm represents a spectral region in which the excitation power is too low for reliable power dependence to be obtained. A multiplicative factor common to the two- and three-photon spectra is chosen to normalize the two-photon spectrum to the absolutely determined value at 1040 nm.

V. DISCUSSION

A. Physical interpretation of the multiphoton spectrum

The excitation spectrum of Fig. 8 possesses a number of interesting features that hint at the underlying physics of the Si-V defect. First, the spectrum displays no visible peak at twice the one-photon ZPL wavelength (1476 nm), which is consistent with $D_{3\mathrm{D}}$ symmetry of the Si-V center, which does not permit a pure two-photon transition between the ^2E_u excited and ^2E_g ground states. Interaction with parity-odd phonons could still allow enhanced two-photon absorption near twice the ZPL wavelength, but our spectrum does not display any noticeable phonon sideband in the spectral region below 1476 nm. Our excitation spectrum also shows a considerable increase in two-photon-excited fluorescence at the short-wavelength end of the spectrum. A possible explanation is excitation to the continuum, but *ab initio* calculations [18] indicate that the depth of the Si-V levels below the conduction band is too great to explain the observed increase. Alternative explanations of the increased two-photon-excited emission at shorter wavelengths are excitation via another, previously unknown bound level, most likely of even parity, or resonant enhancement of the two-photon absorption by the intermediate ^2E_u excited state. We also note a small bump in the two-photon excitation spectrum around 1200 nm, which may reflect direct two-photon excitation on the ^2E_g to the $^2A_{1g}$ transition; a transition between these levels would be two-photon allowed even in the absence of

phonons. A thorough elucidation of the origins of the observed spectral dependence and that of the observed three-photon absorption, including a more detailed treatment of the role of symmetry, will require further investigation.

B. Prospects for deep-tissue imaging

When detecting a fluorophore in the presence of a large background signal, such as autofluorescence from biological tissue, the practical detection limit for a given integration time is defined by the condition that the detected signal from the label must exceed the noise from the background. Since background light outside the spectral bandwidth of the signal of interest can, in principle, be rejected via spectral filtering, the relevant shot-noise-limited background noise is proportional to the square root of the emission linewidth. Thus, the shot-noise-limited figure of merit $\mathcal{M}$ for an optical label in deep-tissue molecular imaging is approximately given by the fluorescence cross section divided by the square root of the linewidth,

$$\mathcal{M} = \frac{\sigma_{\text{fluor}}}{\sqrt{\gamma}}. \tag{11}$$

Using this figure of merit, we can predict the relative performance of similar types of labels for deep-tissue imaging. For instance, two-photon excitation of N-V centers in diamond were measured by Wee *et al.* [45] to have a two-photon absorption cross section of 0.45 GM (corresponding to a two-photon fluorescence cross section of around 0.32 GM), and the N-V emission linewidth is approximately 100 nm. Our measured Si-V ZPL linewidth is 5.6 nm; Neu *et al.* [46] observed room-temperature linewidths as small as 0.7 nm in a Si-V center–containing nanodiamonds grown on iridium, though such narrow linewidths have not, to our knowledge, been observed in bulk diamond or in other nanodiamond samples. Consequently, our measurements suggest that the figure of merit of a Si-V defect label, with a two-photon cross section of 0.74 GM at 1040 nm and linewidths of 0.7 to 5 nm, is between 10 and 30 times larger than that of a N-V defect, pointing to a bright future for silicon-vacancy-doped diamond two-photon labels in applications where their photo- and chemical stability are of key importance. Our spectral measurements indicate that the figure of merit can be enhanced further by tuning the excitation laser toward 900 nm. Furthermore, the narrowness of the Si-V ZPL offers greater potential for spectral multiplexing in combination with labels such as the recently discovered narrow-line germanium vacancy defects [47] or the large number of other known defects in diamond [48,49].

Also important in an evaluation of the prospects of Si-V defect-containing diamond labels is an assessment of the ease of producing nanoparticle labels containing a high density of color centers. We study the achievable density of Si-V color centers by systematically varying the implantation dose and measuring the Si-V one-photon fluorescence, as shown in Fig. 9. Our measurements show a maximum of around $n_{2D} = 3 \times 10^{11}$ cm^{-2} in the density of silicon vacancies produced as a function of the implantation ion dose, as shown in Fig. 9. Assuming, based on our SRIM simulation results, that these vacancies are quasiuniformly distributed over a depth of 1 μm, the three-dimensional number density is then $n_{3D} \approx 3 \times 10^{15}$ cm^{-3}, or 17 ppb. This density is substantially (about 10^3 times) lower than that achieved for N-V centers [50]. However, work by D'Haenens-Johansson *et al.* [51] has shown densities of neutrally charged Si-V centers with densities around 10^{17} cm^{-3}, while Vlasov *et al.* [52] have shown that silicon vacancies can exist stably in nanodiamonds as small as 2 nm in diameter, corresponding to a single-nanodiamond density of over 10^{20} cm^{-3}. Evans *et al.* [53] have moreover demonstrated that strain-induced line broadening of Si-V centers in implanted nanodiamond samples can be greatly decreased via careful high-temperature annealing, reducing the inhomogeneous broadening from approximately 5 nm to as little as 0.03 nm. Based on these observations, we believe that much higher Si-V densities are likely to be achievable following additional optimization of the growth or implantation and annealing steps, allowing realization of bright two-photon Si-V nanodiamond labels.

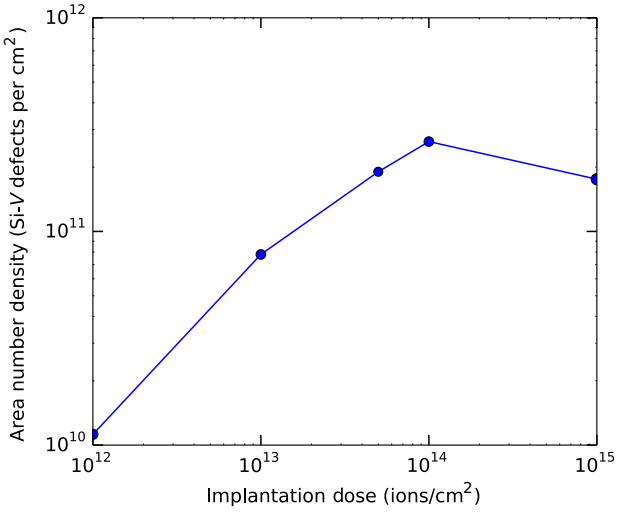

FIG. 9. Number density of silicon vacancies postannealing as a function of the implantation ion dose.

VI. CONCLUSION

In this work, we measure the two-photon cross section of the negatively charged silicon-vacancy color center in diamond at an excitation wavelength of 1040 nm. Our results yield an absolute determination of the two-photon silicon-vacancy cross section at 1040 nm equal to approximately 0.74 GM. We measure the wavelength dependence of the two-photon fluorescence cross section, finding a

significant increase of the cross section for the shortest wavelengths measured. Finally, we assess two-photon-interrogated Si-V–containing diamonds as a bright nonbleaching biological label for deep-tissue imaging, and we find that its expected performance significantly exceeds that of N-V centers in diamond, provided that Si-V nanodiamonds can be produced with defect densities comparable to N-V nanodiamonds. Our result shows that two-photon-excited Si-V-nanodiamond labels offer an outstanding combination of brightness, narrow-line emission, and photostability. These characteristics promise improved sensitivity, greater detection depth, and longer interrogation times in long-term cell tracking and *in vivo* molecular-imaging experiments, with significant applications to many topics of fundamental biological and biomedical interest, including drug efficacy testing, studies of circulating tumor cells, and immune-cell trafficking.

APPENDIX A: CALCULATION OF COLLECTION EFFICIENCY

In the experimental apparatus, the light emitted by the fluorophore must escape from the diamond substrate before being collected and transmitted by the objective. We compute the fraction of the total fluorescence emitted by the color center that enters the objective as follows:

$$\eta_{\mathrm{coll}} = \frac{\sum_i \int d\Omega \frac{d\mathcal{F}_i}{d\Omega} T_i}{\sum_i \int d\Omega \frac{d\mathcal{F}_i}{d\Omega}}, \tag{A1}$$

where $d\mathcal{F}_i/d\Omega$ is the fluorescence power emitted per solid angle, T_i is the Fresnel transmission probability at the diamond-air interface for polarization i, and the integration in the numerator is over the solid angle defined by the numerical aperture of the objective. As shown below, the calculated collection efficiency is the same, whether we assume isotropic emission or dipole emission from a dipole oriented along the $\langle 111 \rangle$ direction of the diamond lattice.

1. Calculation for isotropic emission

If the color center emits isotropic, unpolarized radiation, the collection efficiency simplifies to

$$\eta_{\mathrm{coll}} = \frac{1}{4}\int_0^{\theta_{\max}} \sin\theta d\theta [T_S(\theta) + T_P(\theta)], \tag{A2}$$

where the maximum collection angle is defined by the numerical aperture of the collection objective, i.e., $n\sin\theta_{\max} = \mathrm{NA}$, n is the index of refraction of diamond, and the transmission coefficients from diamond into air for S and P polarization are

$$T_S = \frac{n\cos\theta - \sqrt{1 - n^2\sin^2\theta}}{n\cos\theta + \sqrt{1 - n^2\sin^2\theta}} \tag{A3}$$

and

$$T_P = \frac{n\sqrt{1 - n^2\sin^2\theta} - \cos\theta}{n\sqrt{1 - n^2\sin^2\theta} + \cos\theta}. \tag{A4}$$

Equation (A2) can be integrated numerically, using a diamond dielectric constant of $n = 2.42$ and a numerical aperture (NA) of 0.75, implying an angle $\theta_{\max} \approx 0.315$ rad, resulting in a collection efficiency $\eta_{\mathrm{coll}} \approx 0.0203$.

2. Calculation for dipole emission

The dipole-emission amplitude along direction $\hat{n}$ due to a dipole oscillating along axis $\hat{p}$ is proportional to $\hat{n}\times(\hat{n}\times\hat{p}) = \hat{n}(\hat{n}\cdot\hat{p}) - \hat{p}$. Here, we take $\hat{p} = (1/\sqrt{3})(\hat{x} + \hat{y} + \hat{z})$, with the origin of spherical coordinates at the color center and the polar axis normal to the diamond-air interface. The two polarization axes are $\hat{\phi} = -\sin\phi\hat{x} + \cos\phi\hat{y}$ and $\hat{\theta} = \cos\theta\cos\phi\hat{x} + \cos\theta\sin\phi\hat{y} - \sin\theta\hat{z}$, corresponding to S and P polarization at the interface. Thus, the amplitudes for emission with these polarizations are, respectively,

$$\mathcal{A}_S = -\alpha\hat{\phi}\cdot\hat{p} = -\frac{\alpha}{\sqrt{3}}(\cos\phi - \sin\phi) \tag{A5}$$

and

$$\mathcal{A}_S = -\alpha\hat{\theta}\cdot\hat{p} = -\frac{\alpha}{\sqrt{3}}[\cos\theta(\cos\phi + \sin\phi) - \sin\theta], \tag{A6}$$

where α is a proportionality constant, and where we use the fact that $\hat{n}$ is orthogonal to both polarization unit vectors. The proportionality constant is determined to be $\alpha = \sqrt{3/8\pi}$ by normalizing to unit probability. Thus, the total collection efficiency is given by

$$\eta_{\mathrm{coll,dipole}} = \int_0^{\theta_{\max}} \sin\theta d\theta \int_0^{2\pi} d\phi\ldots \times [|\mathcal{A}_S|^2 T_S(\theta) + |\mathcal{A}_P|^2 T_P(\theta)]. \tag{A7}$$

Simplifying the integral for $\eta_{\mathrm{coll,dipole}}$, we obtain

$$\begin{aligned}\eta_{\mathrm{coll,dipole}} = \frac{1}{8\pi}\int_0^{\theta_{\max}} \sin\theta d\theta \int_0^{2\pi} d\phi\ldots \\ \times\{[1 + 2\cos\theta\sin\phi\cos\phi\ldots \\ - 2\sin\theta\cos\theta(\cos\phi + \sin\phi)]T_P(\theta)\ldots \\ + (1 - 2\sin\phi\cos\phi)T_S(\theta)\}.\end{aligned} \tag{A8}$$

Noting that the transmission coefficients depend only on θ, we can perform the ϕ integral; terms in the integrand proportional to $\sin\phi$,$\cos\phi$, and $\sin\phi\cos\phi$ vanish by symmetry, and we obtain

$$\eta_{\mathrm{coll,dipole}} = \frac{1}{8\pi}\int_0^{\theta_{\max}} \sin\theta d\theta \int_0^{2\pi} d\phi \ldots [T_S(\theta) + T_P(\theta)]$$
$$= \frac{1}{4}\int_0^{\theta_{\max}} \sin\theta d\theta [T_S(\theta) + T_P(\theta)]. \quad \text{(A9)}$$

It is interesting to note that the collection efficiency is identical to the isotropic case, and that this equality obtains only for a dipole oriented at an angle of $\cos^{-1}(1/\sqrt{3})$ to the surface normal.

For color centers within approximately a half wavelength of the surface, the Purcell effect modifies the spontaneous emission rate, and thus the detected fluorescence [54]. For our samples, simulations of the implantation process indicate a defect depth that peaks at around 1 μm and, consequently, a negligible Purcell enhancement of the fluorescence rate.

APPENDIX B: PULSE-WIDTH MEASUREMENT

The pulse width is measured by means of an autocorrelator, as described in Ref. [55]. In a simple model (e.g., neglecting pulse chirp), the electric field for a single pulse incident on the autocorrelator is assumed to be of the form

$$E = E_0 e^{-i\omega_0 t} e^{-t^2/2\tau^2}. \quad \text{(B1)}$$

The electric field at the output port of the Michelson interferometer is then

$$E = E_0' e^{-i\omega_0 t} e^{-t^2/2\tau^2} + E_0' e^{i\Delta\phi} e^{-i\omega_0 t} e^{-(t-2\Delta x/c)^2/2\tau^2}, \quad \text{(B2)}$$

where $\Delta\phi$ incorporates the phase difference $2k\Delta x$ due to the mirror displacement Δx, as well as any static phase difference between the two paths. The intensity corresponding to this output field is then of the form

$$I = I_0[e^{-t^2/\tau^2} + e^{-(t-2\Delta x/c)^2/\tau^2} + \cdots$$
$$\times 2\cos(\Delta\phi) e^{-t^2/2\tau^2} e^{-(t-2\Delta x/c)^2/2\tau^2}]$$
$$= I_0 e^{-t^2/\tau^2}[1 + e^{4t\Delta x/c\tau^2 - 4\Delta x^2/c^2\tau^2} + \cdots$$
$$\times 2\cos(\Delta\phi) e^{2t\Delta x/c\tau^2 - 2\Delta x^2/c^2\tau^2}]. \quad \text{(B3)}$$

The total signal detected at the photodiode is proportional by design to the square of the time-averaged intensity, i.e., to the time integral of the I^2. Performing this integration yields a photodiode signal S, given by

$$S = S_0(1 + e^{-2\Delta x^2/c^2\tau^2} + 4\cos\Delta\phi e^{-3\Delta x^2/2c^2\tau^2} \cdots$$
$$+ 2\cos^2\Delta\phi e^{-2\Delta x^2/c^2\tau^2}). \quad \text{(B4)}$$

The upper envelope of the oscillatory curve given by this expression as a function of Δx is

$$S_+ = S_0(1 + 3e^{-2\Delta x^2/c^2\tau^2} + 4e^{-3\Delta x^2/2c^2\tau^2}), \quad \text{(B5)}$$

while the lower envelope is

$$S_- = S_0(1 + 3e^{-2\Delta x^2/c^2\tau^2} - 4e^{-3\Delta x^2/2c^2\tau^2}). \quad \text{(B6)}$$

Consequently, the difference envelope is given by a pure Gaussian,

$$\Delta S \equiv S_+ - S_- = 8S_0 e^{-3\Delta x^2/2c^2\tau^2}. \quad \text{(B7)}$$

The spatial period of the oscillatory waveform enclosed by these envelopes is $\lambda/2$, corresponding to a relative pulse time delay of $\lambda/2c$.

When this signal is recorded on an oscilloscope as a function of time, the position is assumed to be a linear function of time, $\Delta x = \alpha t$. Thus, the temporal period T of the oscilloscope trace is given by $T = \lambda/2\alpha$, or $\alpha = \lambda/2T$. The 1/e half width $t_{1/e}$ of a Gaussian fit to ΔS occurs when

$$3\alpha^2 t_{1/e}^2/2c^2\tau^2 = 1 \quad \text{(B8)}$$

or

$$\tau = \sqrt{\frac{3}{8}}\frac{\lambda t_{1/e}}{cT}. \quad \text{(B9)}$$

The difference envelope obtained from an autocorrelator measurement on our 1040-nm laser and a Gaussian fit to the difference envelope are shown in Fig. 10.

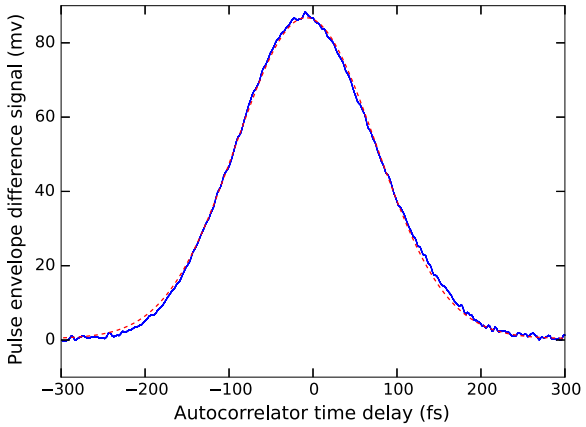

FIG. 10. Autocorrelator waveform difference envelope ΔS. The blue curve is obtained from the autocorrelator oscilloscope trace by numerically locating the maxima and minima of the filtered waveform. A nonuniform interpolation in time is performed to approximately linearize the quasisinusoidal motion of the interferometer mirror. The horizontal axis is calibrated by relating the period of oscillation of the waveform to the optical oscillation period. The dashed red curve is a Gaussian fit to the data. The true laser-pulse width τ is $\sqrt{3/8}$ times the fitted width of this curve, or 72 fs.

APPENDIX C: MEASUREMENT IN DENSE SAMPLE

If the color centers whose fluorescence is to be collected are present on a surface with a certain area number density $n_{2D}(x,y)$, and the excitation laser beam has a transverse spatial profile given by the function $I(x,y) \equiv I_0 F_{ex}(x,y)$, with a spatial maximum I_0 at the center of the excitation beam, then the observed signal is given by

$$\Gamma_{det,2p} = \sigma_{2p} \int dxdy\, \eta_{det} G(x,y) n_{2D}(x,y) \langle I^2(x,y) \rangle, \quad \text{(C1)}$$

where $\eta_{det} G(x,y)$ is the spatially dependent detection efficiency and G is the detection PSF of the microscope, equal to the convolution of the confocal pinhole aperture function and the imaging point-spread function at the detection wavelength. To avoid ambiguity, we choose G to be a unit-maximum function and to include the finite on-axis transmission of the pinhole $\eta_{pinhole}$ as one of several factors contributing to η_{det}. In other words,

$$\eta_{pinhole} G(x,y) \equiv \int dx'dy' G_0(x'-x, y'-y) H(x',y'), \quad \text{(C2)}$$

where G_0 is the PSF in the absence of any pinhole. Simplifying under the assumption that the fluorophore density is uniform, we obtain

$$\Gamma_{det,2p} = \eta_{det} \sigma_{2p} \langle I_0^2 \rangle n_{2D} A_2,$$

where A_2 is an effective area defined by the spatial overlap of the detection point-spread function and the square of the excitation point-spread function as

$$A_2 \equiv \int dxdy\; G(x,y) F_{ex}^2(x,y). \quad \text{(C3)}$$

The time-averaged square intensity for a train of Gaussian-envelope pulses is related to the average intensity by Eq. (3). Hence, for such a pulse train, the average detection rate is given by

$$\Gamma_{det,2p} = \eta_{det} \sigma_{2p} \langle I_0 \rangle^2 n_{2D} A_2 \frac{T_{rep}}{\tau\sqrt{2\pi}}. \quad \text{(C4)}$$

The total excitation power measured by a power meter is related to the intensity at the focus by Eq. (4). Thus, the detected signal is given in terms of the average excitation laser power by

$$\Gamma_{det,2p} = \eta_{det} \sigma_{2p} n_{2D} A_2 \left(\frac{\langle P \rangle}{A_{ex}} \right)^2 \frac{T_{rep}}{\tau\sqrt{2\pi}}.$$

For three-photon excitation, the calculation is very similar and results in the relation

$$\Gamma_{det,3p} = \eta_{det} \sigma_{3p} n_{2D} \left(\frac{\langle P \rangle}{A_{ex}} \right)^3 \frac{T_{rep}^2 A_3}{\pi\tau^2\sqrt{3}},$$

where

$$A_3 \equiv \int dxdy G(x,y) F_{ex}^3(x,y).$$

[1] G. Balasubramanian, I. Chan, R. Kolesov, M. Al-Hmoud, J. Tisler, C. Shin, C. Kim, A. Wojcik, P. R. Hemmer, A. Krueger, T. Hanke, A. Leitenstorfer, R. Bratschitsch, F. Jelezko, and J. Wrachtrup, Nanoscale imaging magnetometry with diamond spins under ambient conditions, Nature (London) **455**, 648 (2008).

[2] J. Maze, P. Stanwix, J. Hodges, S. Hong, J. Taylor, P. Cappellaro, L. Jiang, M. G. Dutt, E. Togan, A. Zibrov, A. A. Yacoby, R. L. Walsworth, and M. D. Lukin, Nanoscale magnetic sensing with an individual electronic spin in diamond, Nature (London) **455**, 644 (2008).

[3] J. Taylor, P. Cappellaro, L. Childress, L. Jiang, D. Budker, P. Hemmer, A. Yacoby, R. Walsworth, and M. Lukin, High-sensitivity diamond magnetometer with nanoscale resolution, Nat. Phys. **4**, 810 (2008).

[4] V. Acosta, E. Bauch, A. Jarmola, L. Zipp, M. Ledbetter, and D. Budker, Broadband magnetometry by infrared-absorption detection of nitrogen-vacancy ensembles in diamond, Appl. Phys. Lett. **97**, 174104 (2010).

[5] P. Maletinsky, S. Hong, M. S. Grinolds, B. Hausmann, M. D. Lukin, R. L. Walsworth, M. Loncar, and A. Yacoby, A robust scanning diamond sensor for nanoscale imaging with single nitrogen-vacancy centres, Nat. Nanotechnol. **7**, 320 (2012).

[6] H. Mamin, M. Kim, M. Sherwood, C. Rettner, K. Ohno, D. Awschalom, and D. Rugar, Nanoscale nuclear magnetic resonance with a nitrogen-vacancy spin sensor, Science **339**, 557 (2013).

[7] T. Staudacher, F. Shi, S. Pezzagna, J. Meijer, J. Du, C. Meriles, F. Reinhard, and J. Wrachtrup, Nuclear magnetic resonance spectroscopy on a (5-nanometer) 3 sample volume, Science **339**, 561 (2013).

[8] M. G. Dutt, L. Childress, L. Jiang, E. Togan, J. Maze, F. Jelezko, A. Zibrov, P. Hemmer, and M. Lukin, Quantum register based on individual electronic and nuclear spin qubits in diamond, Science **316**, 1312 (2007).

[9] P. Neumann, N. Mizuochi, F. Rempp, P. Hemmer, H. Watanabe, S. Yamasaki, V. Jacques, T. Gaebel, F. Jelezko, and J. Wrachtrup, Multipartite entanglement among single spins in diamond, Science **320**, 1326 (2008).

[10] C. Santori, P. E. Barclay, K. M. C. Fu, R. G. Beausoleil, S. Spillane, and M. Fisch, Nanophotonics for quantum optics using nitrogen-vacancy centers in diamond, Nanotechnology **21**, 274008 (2010).

[11] G. D. Fuchs, G. Burkard, P. V. Klimov, and D. D. Awschalom, A quantum memory intrinsic to single nitrogen-vacancy centres in diamond, Nat. Phys. **7**, 789 (2011).
[12] A. Faraon, C. Santori, Z. Huang, V. M. Acosta, and R. G. Beausoleil, Coupling of Nitrogen-Vacancy Centers to Photonic Crystal Cavities in Monocrystalline Diamond, Phys. Rev. Lett. **109**, 033604 (2012).
[13] L. Childress and R. Hanson, Diamond N-*V* centers for quantum computing and quantum networks, MRS Bull. **38**, 134 (2013).
[14] V. Vaijayanthimala, P.-Y. Cheng, S.-H. Yeh, K.-K. Liu, C.-H. Hsiao, J.-I. Chao, and H.-C. Chang, The long-term stability and biocompatibility of fluorescent nanodiamond as an *in vivo* contrast agent, Biomaterials **33**, 7794 (2012).
[15] R. Igarashi, Y. Yoshinari, H. Yokota, T. Sugi, F. Sugihara, K. Ikeda, H. Sumiya, S. Tsuji, I. Mori, H. Tochio, Y. Harada, and M. Shirakawa, Real-time background-free selective imaging of fluorescent nanodiamonds *in vivo*, Nano Lett. **12**, 5726 (2012).
[16] H. Sternschulte, K. Thonke, R. Sauer, P. C. Münzinger, and P. Michler, 1.681-eV luminescence center in chemical-vapor-deposited homoepitaxial diamond films, Phys. Rev. B **50**, 14554 (1994).
[17] C. D. Clark, H. Kanda, I. Kiflawi, and G. Sittas, Silicon defects in diamond, Phys. Rev. B **51**, 16681 (1995).
[18] J. P. Goss, R. Jones, S. J. Breuer, P. R. Briddon, and S. Öberg, The Twelve-Line 1.682 eV Luminescence Center in Diamond and the Vacancy-Silicon Complex, Phys. Rev. Lett. **77**, 3041 (1996).
[19] L. J. Rogers, K. D. Jahnke, M. W. Doherty, A. Dietrich, L. P. McGuinness, C. Müller, T. Teraji, H. Sumiya, J. Isoya, N. B. Manson, and F. Jelezko, Electronic structure of the negatively charged silicon-vacancy center in diamond, Phys. Rev. B **89**, 235101 (2014).
[20] E. Neu, C. Hepp, M. Hauschild, S. Gsell, M. Fischer, H. Sternschulte, D. Steinmüller-Nethl, M. Schreck, and C. Becher, Low-temperature investigations of single silicon vacancy colour centres in diamond, New J. Phys. **15**, 043005 (2013).
[21] E. Neu, M. Agio, and C. Becher, Photophysics of single silicon vacancy centers in diamond: Implications for single photon emission, Opt. Express **20**, 19956 (2012).
[22] C. Hepp, T. Müller, V. Waselowski, J. N. Becker, B. Pingault, H. Sternschulte, D. Steinmüller-Nethl, A. Gali, J. R. Maze, M. Atatüre, and C. Becher, Electronic Structure of the Silicon Vacancy Color Center in Diamond, Phys. Rev. Lett. **112**, 036405 (2014).
[23] T. D. Merson, S. Castelletto, I. Aharonovich, A. Turbic, T. J. Kilpatrick, and A. M. Turnley, Nanodiamonds with silicon vacancy defects for nontoxic photostable fluorescent labeling of neural precursor cells, Opt. Lett. **38**, 4170 (2013).
[24] A. T. Collins, L. Allers, C. J. Wort, and G. A. Scarsbrook, The annealing of radiation damage in de Beers colourless CVD diamond, Diamond Relat. Mater. **3**, 932 (1994).
[25] J.-H. Lee, Y.-M. Huh, Y.-w. Jun, J.-w. Seo, J.-t. Jang, H.-T. Song, S. Kim, E.-J. Cho, H.-G. Yoon, J.-S. Suh *et al.*, Artificially engineered magnetic nanoparticles for ultra-sensitive molecular imaging, Nat. Med. **13**, 95 (2007).
[26] V. Ntziachristos, C. Bremer, and R. Weissleder, Fluorescence imaging with near-infrared light: New technological advances that enable *in vivo* molecular imaging, European Journal of Radiology **13**, 195 (2003).
[27] X. Gao, L. Yang, J. A. Petros, F. F. Marshall, J. W. Simons, and S. Nie, *In vivo* molecular and cellular imaging with quantum dots, Curr. Opin. Biotechnol. **16**, 63 (2005).
[28] X. Michalet, F. Pinaud, L. Bentolila, J. Tsay, S. Doose, J. Li, G. Sundaresan, A. Wu, S. Gambhir, and S. Weiss, Quantum dots for live cells, *in vivo* imaging, and diagnostics, Science **307**, 538 (2005).
[29] P.-H. Chung, E. Perevedentseva, J.-S. Tu, C. Chang, and C.-L. Cheng, Spectroscopic study of bio-functionalized nanodiamonds, Diamond Relat. Mater. **15**, 622 (2006).
[30] N. Mohan, C.-S. Chen, H.-H. Hsieh, Y.-C. Wu, and H.-C. Chang, *in vivo* imaging and toxicity assessments of fluorescent nanodiamonds in caenorhabditis elegans, Nano Lett. **10**, 3692 (2010).
[31] X. Qian, X.-H. Peng, D. O. Ansari, Q. Yin-Goen, G. Z. Chen, D. M. Shin, L. Yang, A. N. Young, M. D. Wang, and S. Nie, *in vivo* tumor targeting and spectroscopic detection with surface-enhanced Raman nanoparticle tags, Nat. Biotechnol. **26**, 83 (2008).
[32] C. L. Zavaleta, B. R. Smith, I. Walton, W. Doering, G. Davis, B. Shojaei, M. J. Natan, and S. S. Gambhir, Multiplexed imaging of surface enhanced Raman scattering nanotags in living mice using noninvasive Raman spectroscopy, Proc. Natl. Acad. Sci. U.S.A. **106**, 13511 (2009).
[33] F. Helmchen and W. Denk, Deep tissue two-photon microscopy, Nat. Methods **2**, 932 (2005).
[34] K. Svoboda and R. Yasuda, Principles of two-photon excitation microscopy and its applications to neuroscience, Neuron **50**, 823 (2006).
[35] C. Xu and W. W. Webb, Measurement of two-photon excitation cross sections of molecular fluorophores with data from 690 to 1050 nm, J. Opt. Soc. Am. B **13**, 481 (1996).
[36] M. Drobizhev, N. S. Makarov, S. E. Tillo, T. E. Hughes, and A. Rebane, Two-photon absorption properties of fluorescent proteins, Nat. Methods **8**, 393 (2011).
[37] A. M. Smith, M. C. Mancini, and S. Nie, Bioimaging: Second window for *in vivo* imaging, Nat. Nanotechnol. **4**, 710 (2009).
[38] J. Song, H. Li, F. Lin, L. Wang, H. Wu, and Y. Yang, Plasmon-enhanced photoluminescence of Si-*V* centers in diamond from a nanoassembled metal-diamond hybrid structure, CrystEngComm **16**, 8356 (2014).
[39] A. Batalov, V. Jacques, F. Kaiser, P. Siyushev, P. Neumann, L. J. Rogers, R. L. McMurtrie, N. B. Manson, F. Jelezko, and J. Wrachtrup, Low Temperature Studies of the Excited-State Structure of Negatively Charged Nitrogen-Vacancy Color Centers in Diamond, Phys. Rev. Lett. **102**, 195506 (2009).
[40] J. F. Ziegler, M. D. Ziegler, and J. P. Biersack, SRIM—The stopping and range of ions in matter (2010), Nucl. Instrum. Methods Phys. Res., Sect. B **268**, 1818 (2010).
[41] E. Neu, M. Fischer, S. Gsell, M. Schreck, and C. Becher, Fluorescence and polarization spectroscopy of single silicon vacancy centers in heteroepitaxial nanodiamonds on iridium, Phys. Rev. B **84**, 205211 (2011).

[42] C. Wang, C. Kurtsiefer, H. Weinfurter, and B. Burchard, Single photon emission from Si-*V* centres in diamond produced by ion implantation, J. Phys. B **39**, 37 (2006).

[43] I. I. Vlasov, A. S. Barnard, V. G. Ralchenko, O. I. Lebedev, M. V. Kanzyuba, A. V. Saveliev, V. I. Konov, and E. Goovaerts, Nanodiamond photoemitters based on strong narrow-band luminescence from silicon-vacancy defects, Adv. Mater. **21**, 808 (2009).

[44] L. J. Rogers, K. D. Jahnke, T. Teraji, L. Marseglia, C. Müller, B. Naydenov, H. Schauffert, C. Kranz, J. Isoya, L. P. McGuinness, and F. Jelezko, Multiple intrinsically identical single-photon emitters in the solid state, Nat. Commun. **5**, 4739 (2014).

[45] T.-L. Wee, Y.-K. Tzeng, C.-C. Han, H.-C. Chang, W. Fann, J.-H. Hsu, K.-M. Chen, and Y.-C. Yu, Two-photon excited fluorescence of nitrogen-vacancy centers in proton-irradiated type Ib diamond, J. Phys. Chem. A **111**, 9379 (2007).

[46] E. Neu, D. Steinmetz, J. Riedrich-Möller, S. Gsell, M. Fischer, M. Schreck, and C. Becher, Single photon emission from silicon-vacancy colour centres in chemical vapour deposition nano-diamonds on iridium, New J. Phys. **13**, 025012 (2011).

[47] T. Iwasaki, F. Ishibashi, Y. Miyamoto, Y. Doi, S. Kobayashi, T. Miyazaki, K. Tahara, K.-D. Jahnke, L.-J. Rogers, B. Naydenov, F. Jelezko, S. Yamasaki, S. Nagamachi, T. Inubushi, N. Mizuochi, and M. Hatano, Germanium-vacancy single color centers in diamond, Sci. Rep. **5**, 12882 (2015).

[48] F. Jelezko and J. Wrachtrup, Single defect centres in diamond: A review, Phys. Status Solidi (a) **203**, 3207 (2006).

[49] I. Aharonovich, S. Castelletto, D. Simpson, C. Su, A. Greentree, and S. Prawer, Diamond-based single-photon emitters, Rep. Prog. Phys. **74**, 076501 (2011).

[50] V. Acosta, E. Bauch, M. Ledbetter, C. Santori, K.-M. Fu, P. Barclay, R. Beausoleil, H. Linget, J. Roch, F. Treussart *et al.*, Diamonds with a high density of nitrogen-vacancy centers for magnetometry applications, Phys. Rev. B **80**, 115202 (2009).

[51] U. F. S. D'Haenens-Johansson, A. M. Edmonds, B. L. Green, M. E. Newton, G. Davies, P. M. Martineau, R. U. A. Khan, and D. J. Twitchen, Optical properties of the neutral silicon split-vacancy center in diamond, Phys. Rev. B **84**, 245208 (2011).

[52] I. I. Vlasov, A. A. Shiryaev, T. Rendler, S. Steinert, S.-Y. Lee, D. Antonov, M. Vörös, F. Jelezko, A. V. Fisenko, L. F. Semjonova *et al.*, Molecular-sized fluorescent nanodiamonds, Nat. Nanotechnol. **9**, 54 (2014).

[53] R. E. Evans, A. Sipahigil, D. D. Sukachev, A. S. Zibrov, and M. D. Lukin, Narrow-Linewidth Homogeneous Optical Emitters in Diamond Nanostructures via Silicon Ion Implantation, Phys. Rev. Applied **5**, 044010 (2016).

[54] C. Santori, P. E. Barclay, K.-M. C. Fu, and R. G. Beausoleil, Vertical distribution of nitrogen-vacancy centers in diamond formed by ion implantation and annealing, Phys. Rev. B **79**, 125313 (2009).

[55] J.-C. M. Diels, J. J. Fontaine, I. C. McMichael, and F. Simoni, Control and measurement of ultrashort pulse shapes (in amplitude and phase) with femtosecond accuracy, Appl. Opt. **24**, 1270 (1985).